Self-Powered Broadband Photodetector Based on a Monolayer InSe *p-i-n* Homojunction

Lin Li,[1,2] Peize Yuan,[3] Ting Liu,[1] Zinan Ma,[1] Congxin Xia,[1] and Xueping Li[1,3,*]

[1] *School of Physics, Henan Key Laboratory of Infrared Materials & Spectrum Measures and Applications, Henan Normal University, Xinxiang, Henan 453007, China*

[2] *College of Science, Zhengzhou Key Laboratory of Low-Dimensional Quantum Materials and Devices, Zhongyuan University of Technology, Zhengzhou, 450007, China*

[3] *College of Electronic and Electrical Engineering, Henan Normal University, Xinxiang, Henan 453007, China*

(Received 20 September 2022; revised 4 December 2022; accepted 7 December 2022; published 12 January 2023)

The two-dimensional homojunction is promising in electronic and optoelectronic applications. However, its performance is restricted by lattice mismatch and the depletion region. Here, we construct a monolayer InSe-based *p-i-n* homojunction photodetector. It presents high photoelectric conversion with a wide light response in the photon-energy range from 1.4 to 5 eV, which induces a photocurrent density of 13.13 nA m^{-1} and a photoresponsivity of 0.022 A W^{-1}. Moreover, the gate voltage improves the photocurrent and photoresponsivity almost fourfold. Additionally, the increasing dielectric constant of the substrate decreases the photocurrent spectral width, and a low doping concentration is suitable for photodetectors due to high mobility. These results indicate that the two-dimensional *p-i-n* homojunction is promising for future photoelectric devices.

DOI: 10.1103/PhysRevApplied.19.014039

I. INTRODUCTION

Two-dimensional (2D) lateral junctions can be applied in highly integrated and superior-performance electronic [1–3], optoelectronic [4–8], and synaptic devices [9, 10], due to excellent optoelectronic properties. Recently, 2D high-quality WS_2-WSe_2 [11], MoS_2-WSe_2 [12], $MoSe_2$-WSe_2 [13,14], $2H/1T'$ $MoTe_2$ [15], and monolayer-bilayer WSe_2 [16] lateral heterostructures were studied. Large-area and high-quality-interface $MoSe_2$-WSe_2 lateral heterostructures grown by one-pot chemical vapor deposition synthesis can be applied as rectifiers, photovoltaic cells, and self-powered photodetectors [17]. For the WSe_2-WS_2 lateral-heterostructure-based photodetectors, the zero-gate response time is reduced by 5 orders of magnitude [18]. In addition, the WSe_2-MoS_2 photodetectors also exhibit a large rectification and fast response time [19]. Current studies show that lateral junctions are suited for channel materials of electronic and optoelectronic devices [13,20–22].

Among the many 2D lateral junctions, the homojunction possesses continuous band alignments and a high-quality carrier-diffusion channel for promising device applications [23–26]. For instance, the black-phosphorus homojunction-based photodetector, modulated by the ferroelectric field, demonstrates a large photoresponsivity at room temperature [4]. The bent InSe-formed homojunction manipulates the transport behavior of photogenerated carriers through the flexoelectric polarization potential, which provides the flexophotoelectronic effects in an artificial synaptic device [27]. These outstanding performances of the 2D homojunction are attributed to superior properties at the interface and growth compatibility in designing functional devices.

More recently, Aftab *et al*. demonstrated a $MoTe_2$ lateral *p-i-n* homojunction diode, which presents a higher rectification ratio of about 1.4×10^6 and an open-circuit voltage of 440.9 mV [28]. The WSe_2 homojunction photodetector shows a current *on*:*off* ratio of 1.2×10^6 and a response time of 264 ns [29]. Compared with other lateral homojunctions, the *p-i-n* junction can increase the built-in electric field, extend the depletion region, and weaken the diffuse-carrier influence on the effective region of the photocarrier. The seamless $MoTe_2$ homojunction *p-i-n* diode greatly enhances the photoresponse in the visible-to-1300-nm-wavelength range compared with the *p-n* diode [30]. However, the study of the photoelectric properties of the *p-i-n* homojunction is less reported to date. Meanwhile, many optoelectronic devices based on 2D material are widely studied due to their unique physical properties [31–38]. It is worth noting that 2D InSe is a typical III-VI semiconductor with a moderate band gap of 1.42 eV [39], a small electron effective mass (0.18 m_0) [40], weak electron-phonon scattering, and high electron

*lxpslxhhw@126.com

mobility (10^3 $cm^2\,V^{-1}\,s^{-1}$) [41]. Additionally, InSe has symmetry of the valence and conduction bands as well as the p_z atomic orbital nature, and its exciton states have a large oscillator strength [41–45]. These excellent properties make InSe a strong candidate for designing 2D *p-i-n* junctions. In this work, a monolayer InSe-based *p-i-n* homojunction is designed, and the corresponding electronic structure and photocurrent are systematically explored. To further explore the effective modulation strategy and reveal the underlying mechanism for the effect on the device performance, we study the influence of the electronic band, gate voltage, substrate, and doping concentration on the photocurrent. This work is expected to open a route for realizing 2D *p-i-n* homojunction optoelectronic devices.

II. METHODS

Optimization of the geometric and band structure of monolayer InSe is carried out by using the Vienna *ab initio* simulation package based on density-functional theory (DFT) [46,47]. The Perdew-Burke-Ernzerhof (PBE) functional is chosen to deal with the exchange-correlation interactions [48]. The plane-wave cutoff employed is 500 eV. The energy and force convergence tolerances are set to 10^{-5} eV and 0.01 eV Å^{-1}, respectively. A $5 \times 5 \times 1$ *k*-point mesh is adopted for sampling in reciprocal space. In addition, a vacuum layer of 20 Å in the *z* direction is selected to avoid the interaction between neighboring InSe layers.

The transport property is calculated using the first-principles method in combination with the nonequilibrium Green function, as operated by QuantumATK software [49,50]. The exchange correlation is the PBE functional of the generalized gradient approximation, as well as the norm-conserving pseudopotential, and the basis sets are SG15 and "high" [51–56]. For self-consistency, the *k*-mesh grid is sampled with $1 \times 11 \times 11$ and $1 \times 11 \times 171$ for the left (right) electrode and central region, respectively. A density mesh cutoff of 110 Hartree is applied. Meanwhile, the temperature is set to 300 K [57–60]. The photocurrent calculations use 31 *k* points perpendicular to the transport direction. The photocurrent is calculated using first-order perturbation theory within the first Born approximation [55,61]. The photocurrent, $J_{\rm ph}$, is expressed as

$$J_{\rm ph} = \frac{e}{\hbar}\int \frac{dE}{2\pi}\sum_{k,\alpha} T_\alpha(E,k).$$

The effective transmission coefficients are given by

$$T_\alpha(E,k) = Tr\{i\Gamma_\alpha(E,k)[(1-f_\alpha)G^< + f_\alpha G^>]\},$$

where $G^{>(<)}$ denote the noninteracting Green functions. Γ_α and f_α are the line width and Fermi distribution function of the α (left or right) electrode, respectively.

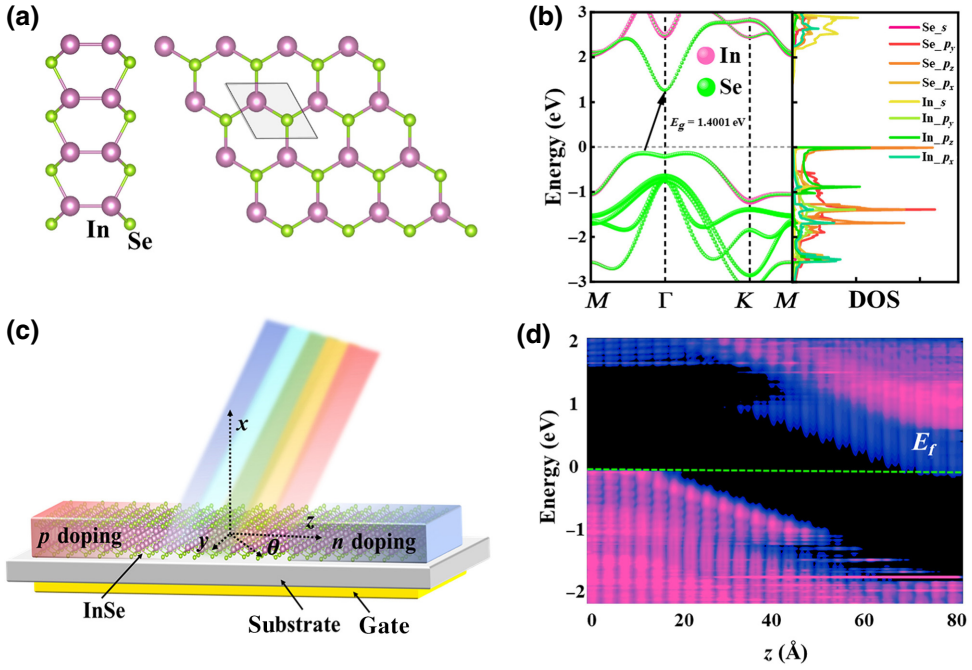

FIG. 1. (a) Side and top views of InSe monolayer atoms. (b) Elemental projected electronic band structures and projected density of states. Monolayer InSe-based *p-i-n* homojunction: (c) sketch and (d) local density of states. Magenta and black represent high and low local density of states, respectively.

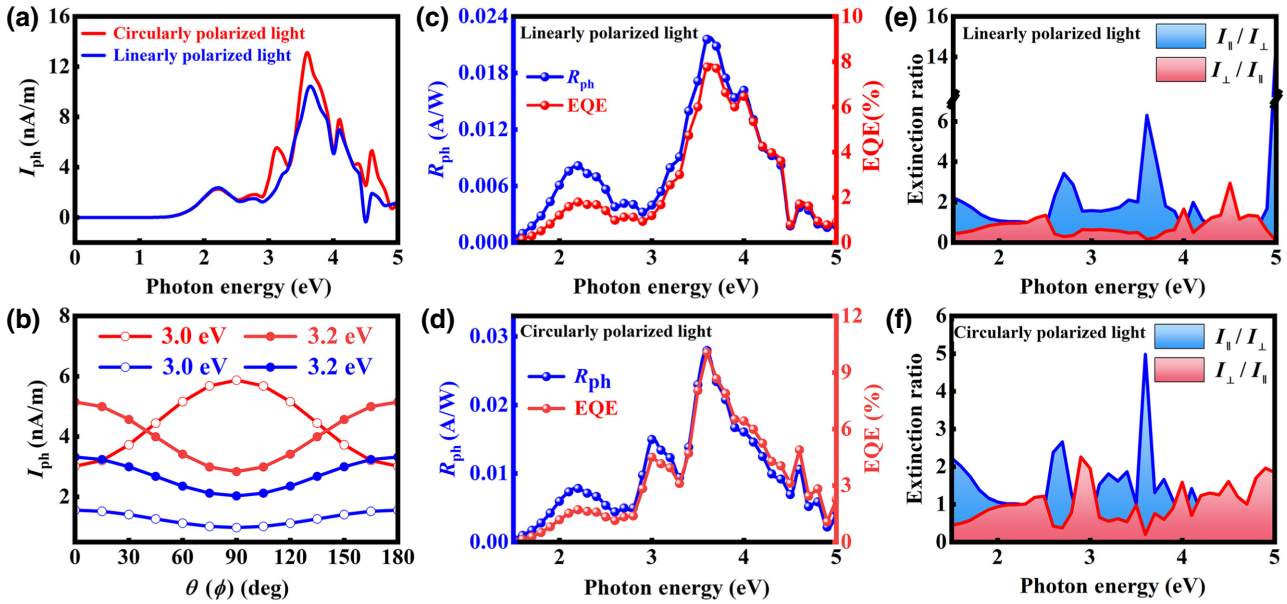

FIG. 2. Photocurrent density as functions of (a) photon energy and (b) θ (ϕ). Red and blue lines represent linearly and circularly polarized light, respectively. (c),(d) R_{ph} and EQE, and (e),(f) extinction ratio of the monolayer InSe *p*-*i*-*n* homojunction.

III. RESULTS AND DISCUSSION

The geometrical atomic structure of the InSe monolayer with a honeycomb lattice is shown in Fig. 1(a), and its lattice constant and thicknesses are 4.09 and 3.57 Å, respectively [62,63]. Additionally, Fig. 1(b) presents an indirect-band-gap characteristic, with 1.4 eV for the InSe monolayer [39]. The projected density of states (DOS) show that the conduction-band minimum (CBM) and the valence-band maximum (VBM) are mainly constituted by the In *p* states and Se *p* states. The VBM has a nonparabolic Mexican-hat-like dispersion with a depression, and the CBM has a steep band edge, which indicates that the electrons have a smaller effective mass than that of holes. We would like to point out that the PBE method underestimates the band value of a semiconductor, while the obtained results can gain the same variation trend with the *GW* and Bethe-Salpeter equation (BSE) methods [51–56]. Therefore, in this manuscript, we employ the PBE method to simulate related properties.

In Fig. 1(c), we sketch the two-probe *p*-*i*-*n* homojunction device based on monolayer InSe, where the source (drain) is doped with acceptor (donor) for the *p*-type (*n*-type) region. The lengths of the *n*- and *p*-doped and central intrinsic regions are 1.7, 1.7, and 5 nm, respectively. The thickness of the substrate is set as 0.41 nm for different 2D transistors. To form flat bands near the electrode, doping concentrations of 9×10^{13} and 1×10^{13} cm^{-2} are chosen for *p*- and *n*-type monolayer InSe, respectively.

Additionally, in Fig. 1(d), the local density of states indicate a typical *p*-*i*-*n* profile, along with the homojunction structure, and the band gap is approximately that of the InSe monolayer. Flat bands near the electrodes represent the existing converged screening potentials, and the curved band means a built-in electric field in the scattering region of the device. Upon light illumination, photoexcited electron-hole pairs are efficiently separated by the built-in electric field in the *p*-*i*-*n* homojunction, which can reduce electron-hole recombination, extend the photocarrier lifetime, and enhance the photocurrent. Accordingly, the *p*-*i*-*n* homojunction can realize a high-performance self-powered photodetector using photogalvanic effects.

In Fig. 2, we discuss the critical factors that characterize the photoelectric properties of the monolayer InSe-based *p*-*i*-*n* homojunction under a normal incidence of polarized light with zero bias, where the entire channel region is vertically irradiated by linearly (or circularly) polarized light illumination (light power density of 16 $\mu W\,mm^{-2}$) and photon energies from 0 to 5 eV. Figure 2(a) shows that the circularly polarized photocurrent density is larger than that of linearly polarized light illumination at the same photon energy. According to Fermi's golden rule [64], the probability of an electron transition is proportional to the DOS. Therefore, the photocurrent density is generated near the photon energy of 1.4 eV, which matches the band gap of InSe. In addition, the maximum photocurrent densities are 10.13 (13.13) $nA\,m^{-1}$ of linearly (circularly) polarized light, which is around the photon energy of 3.6 eV. This originates from the higher transition probability of electrons between the valance band and conduction band, which is excited by the optical absorption of photons with appropriate energy. To further understand the electron transition, we calculate the band structures and

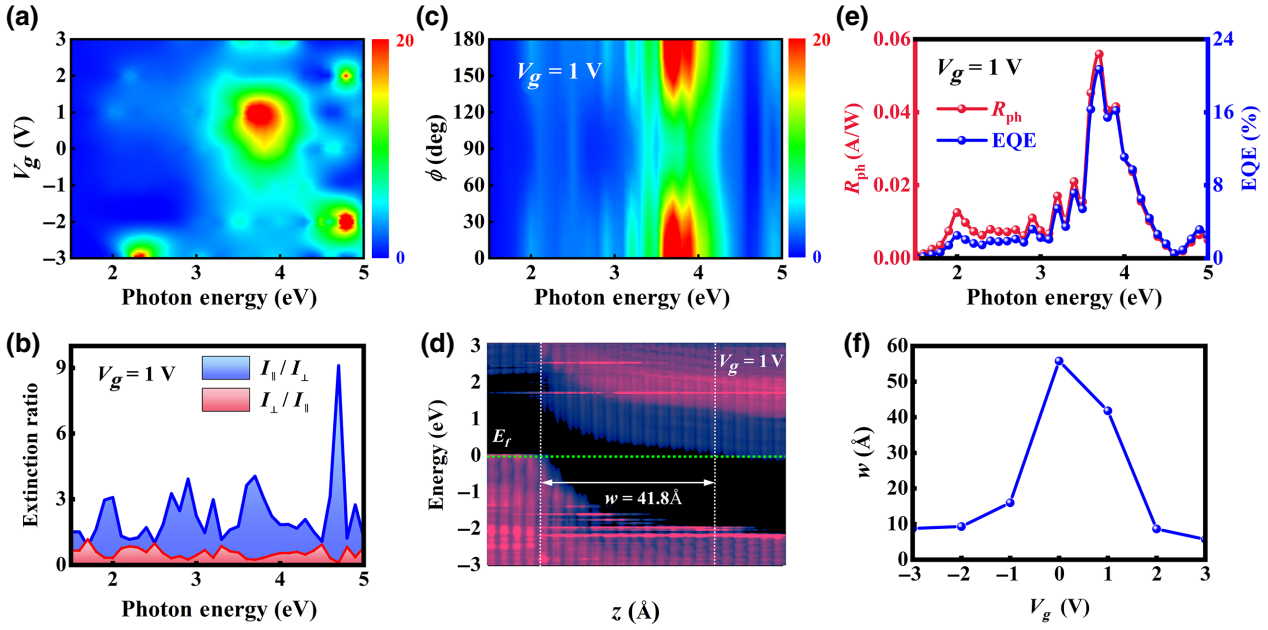

FIG. 3. (a) Gate-dependent and (b) angle-dependent photocurrent-density spectra at different photon energies of the monolayer InSe-based *p-i-n* homojunction under zero bias. (c) R_{ph} and EQE, and (d) extinction ratio at different photon energies. (e) Local density of states under a gate voltage of 1 V. (f) Functional relationship between w and gate voltage.

density of states of monolayer InSe, as given in Fig. 1(b). According to Fermi's golden rule, the DOS peaks (−0.8 and 2.8 eV) can obtain a higher electron-transition rate. In addition, to clarify the contribution of photon energy, we give the optical absorption coefficient in Fig. S1 within the Supplemental Material [65]. There is a prominent

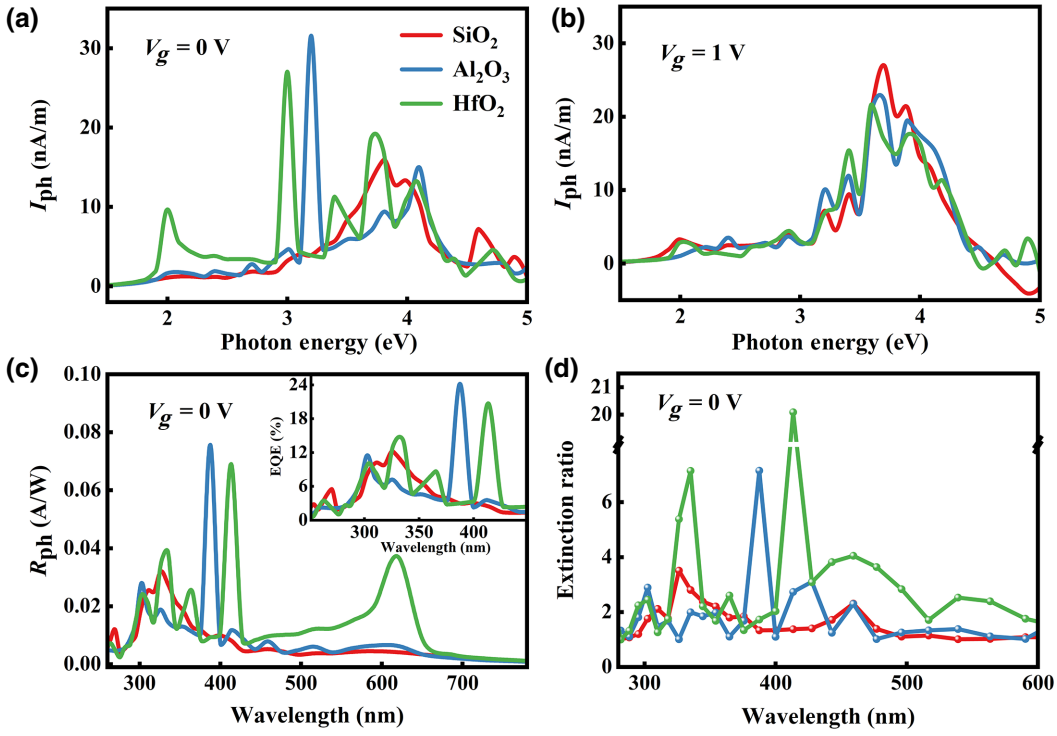

FIG. 4. (a),(b) Photocurrent density and (c),(d) R_{ph}, EQE, and extinction ratio induced by circularly polarized light of the monolayer InSe-based *p-i-n* homojunction with SiO_2, Al_2O_3, and HfO_2 substrates.

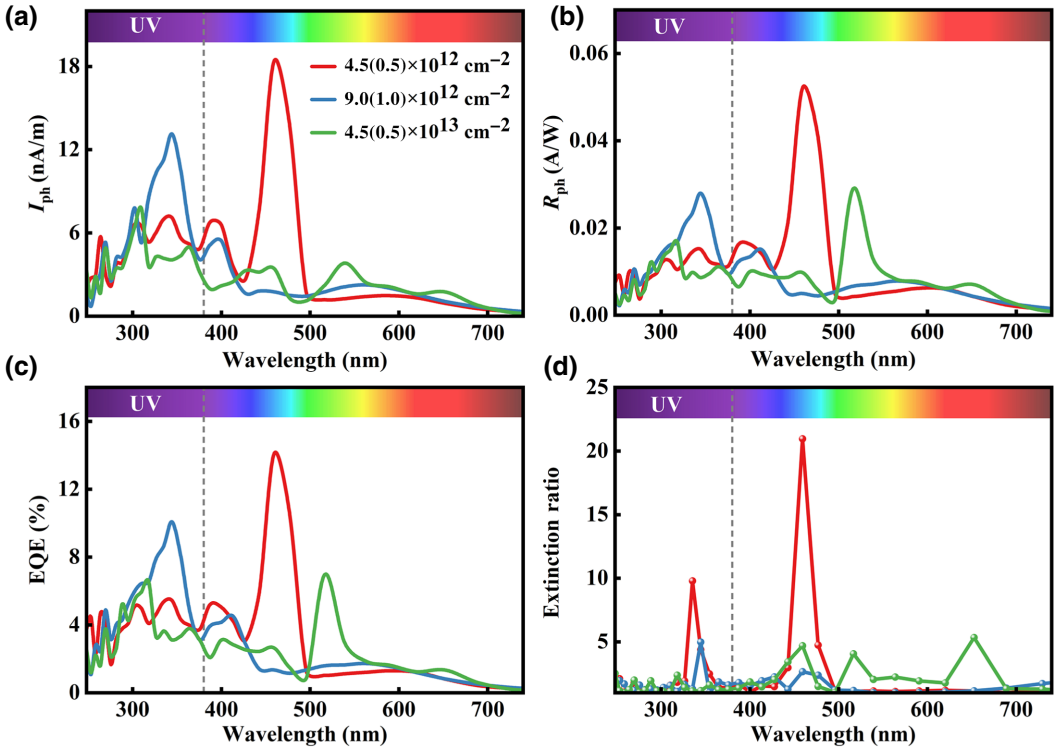

FIG. 5. (a) Photocurrent density, (b) R_{ph}, (c) EQE, and (d) extinction ratio induced by circularly polarized light of the monolayer InSe-based *p-i-n* homojunction with different doping densities.

absorption peak located in the ultraviolet range. Thus, the device absorption of the photon energy of 3.6 eV will produce a large photocurrent.

Additionally, in Fig. 2(b), the photocurrent-density curve presents a perfect sine (cosine) function with polarization angle θ and helicity ϕ, which is consistent with phenomenological theory. Furthermore, to study the influence of incident direction on the photocurrent, we plot the relationship between the photocurrent and photon energies under normal- and grazing-incidence linearly and circularly polarized light, as shown in Fig. S2(a) within the Supplemental Material [65]. Compared with the photocurrent of the two cases, I_{ph} of the grazing-incidence device is larger than that in the normal case. Moreover, the first-maximum value is located at 1.7 and 2.2 eV for the grazing- and normal-incidence devices, respectively. This is because the first direct interband transition is forbidden for normal-incident light, which is consistent with previous work [45]. In addition, Fig. S2(b) within the Supplemental Material [65] further evaluates R_{ph} of the two cases, showing that the grazing-incident light has a large first-maximum R_{ph} located at around 1.7 eV, while it is small beyond the photon energy of 1.8 eV.

As an important indicator of optoelectronics in experiments, Figs. 2(c) and 2(d) depict the photoresponsivity (R_{ph}) and external quantum efficiency (EQE) of linearly and circularly polarized light. R_{ph} characterizes the efficiency of energy conversion and is expressed as $R_{ph} = J_{ph}/PA$, where J_{ph} is the photocurrent, P is the incident-light power density, and A is the effective area. The highest R_{ph} of the *p-i-n* homojunction is about 0.028 (0.022) A W^{-1} under the illumination of linearly (circularly) polarized light in the ultraviolet (UV) emission region, which is comparable with that of 2D-material-based photodetectors (0.015 A W^{-1} for β-AsP, 0.0062 A W^{-1} for black phosphorus, and 0.0101 A W^{-1} for InSe) [66–68]. In addition, the EQE is also an indicator for optoelectronics to evaluate the ratio of extracted free electrons per incident photon flowing out from the device. It is calculated as $E = R_{ph}hc/(e\lambda)$, where λ is the wavelength of light [50,51,56,69]. Figures 2(c) and 2(d) show that the EQE can reach 8% and 10% with linearly and circularly polarized illumination, respectively, which is also bigger than that of β-AsP (6.1%) and the $MoSe_2$-WSe_2 lateral junction (4.3%) [18,67]. Therefore, these performances suggest that the monolayer InSe-based *p-i-n* homojunction has powerful potential for optoelectronic applications.

To assess the polarization influence on the photoelectric property of InSe-based *p-i-n* homojunction photodetectors, the extinction ratio is calculated to evaluate the device sensitivity. It is defined as the maximum value in $R_{\perp}/R_{\parallel}$ and $R_{\parallel}/R_{\perp}$, where $R_{\parallel}$ and $R_{\perp}$ are the photocurrents with polarization angles of 0° and 90° relative to the transmission

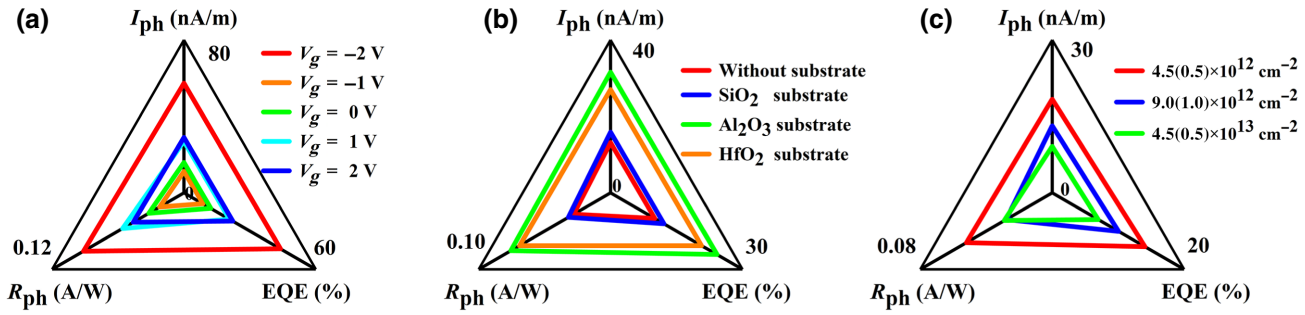

FIG. 6. Photoelectric property of the device with different (a) gate voltages, (b) substrates, and (c) p- (n-) type doping densities.

direction, respectively. Under linearly and circularly polarized illumination, the relationship between the extinction ratio and photon energy can be seen in Figs. 2(e) and 2(f). Large extinction ratios of 6 and 15 at the photon energy of 3.6 and 5.0 eV are obtained for linearly polarized light in Fig. 2(e), and 5 at 3.7 eV for circularly polarized light in Fig. 2(f). In addition, the monolayer InSe-based p-i-n homojunction can be used as a candidate for 2D-material-based photodetectors. Since linearly and circularly polarized light produce similar effects in the device, circularly polarized light is only used to radiate the scattered region in subsequent studies of the photocurrent.

To investigate the gate-voltage modulation of the photocurrent of the monolayer InSe-based p-i-n homojunction, Figs. 3(a) and S3 within the Supplemental Material [65] give the photocurrent density as a function of V_g at 0, ± 1, ± 2, and ± 3 V, where the photon-energy range is from 1.5 to 5 eV. When the gate voltage changes, the photocurrent density is asymmetrically distributed with the photon energy; a larger photocurrent density is generated under lower gate voltages of 1 and -2 V. Taking a gate voltage of 1 V as an example, we also further present the change of photocurrent density with helicity ϕ from 0° to 180° in Figs. 3(b) and S4 within the Supplemental Material [65], showing that the gate voltage can enhance the photocurrent density, which is consistent with phenomenological theory.

Additionally, Fig. 3(c) reveals that R_{ph} and EQE have similar trends and gain maximum values of 0.056 A W^{-1} and 21% around a photon energy of 3.7 eV; these values are larger than that of the monolayer InSe-based p-i-n homojunction without a gate voltage. Moreover, we study the influence of applying a gate voltage on the sensitivity of the devices by the extinction ratio. In Fig. 3(d), a photon energy of 4.7 eV has very large extinction ratios greater than 9. However, the extinction ratio of the photon energy is similar with and without a gate voltage, which means that the extinction ratio is insensitive to gate voltage. To further analyze the underlying physics mechanisms, the local density of states of the device with different gate voltages are shown in Figs. 3(e) and S5 within the Supplemental Material [65]. When the gate voltage is 1 V, the conduction band falls off, leading to the length of the depletion region (w) reducing from 55.8 to 41.8 Å. In Fig. 3(f), w decreases further as the gate voltage increases, which favors the separation of photogenerated electron-hole pairs. Hence, the photocurrent density is enhanced. This indicates that the 2D-material-based p-i-n homojunction with a gate voltage amplifies not only the photocurrent but also keeps the light-radiation effective area.

To explore the substrate effects on photoelectric properties, we choose SiO_2, Al_2O_3, and HfO_2 with dielectric constants of 3.9, 9, and 25, respectively. For comparison with the monolayer InSe-based p-i-n homojunction without the substrate, Figs. 4(a) and 4(b) present the photocurrent-density change with the substrate for gate voltages of 0 and 1 V, showing that the photocurrent density increases. This is because of different charges distributed in the interface between the channel and substrate. We also present the change of photocurrent density with helicity ϕ from 0 to 180° in Fig. S6 within the Supplemental Material [65], and the result is consistent with phenomenological theory. In Fig. 4(a), the photocurrent spectral width increases as the dielectric constant increases. Also, the maximum photocurrent densities appear at 3.8, 3.3, and 3.0 eV. This indicates that the peak position moves towards low photon energy with an increase of the dielectric constant. In addition, the HfO_2 substrate can produce a larger photocurrent density using a low photon energy. It shows that the substrate influences the device performance. Meanwhile, Fig. 4(b) shows the photocurrent density with a gate voltage of 1 V. However, the spectral width barely changes and the maximum photocurrent value decreases with increasing dielectric constant. That is, the gate voltage presents a greater ability to control the charge distribution in the interface between the channel and substrate. For example, if a gate voltage of 1 V and HfO_2 substrate are used, the device performance is similar to that of the SiO_2 substrate. This suggests that it is better to use SiO_2 as a substrate when designing an optoelectronic phototransistor with a gate voltage.

In Figs. 4(c) and 4(d), we plot the parameters R_{ph}, EQE, and extinction ratio under zero gate voltage as a function of wavelength. In the UV-light region, the three cases have wide photocurrent spectra, which is beneficial for UV detection. In addition, the case of HfO_2 substrate also has a visible-light response, and R_{ph} and EQE reach 0.076 A W^{-1} and 24%, respectively, near the wavelength of 400 nm. Meanwhile, Fig. 4(d) presents an extinction ratio for the HfO_2 substrate of around 3 in the visible region and exhibits a maximum extinction ratio of 20. Because of HfO_2-substrate modulation, the monolayer InSe-based *p-i-n* homojunction is suitable for application in photodetectors with broadband photodetection, high responsivity, and high sensitivity. The results show that the substrate can change the interface charge distribution and change the photoelectric performance of the device.

Next, we explore doping-concentration modulation on the monolayer InSe-based *p-i-n* homojunction, as shown in Figs. 5 and S7 within the Supplemental Material [65]. For three device cases, the *p*-(*n*-) type doping concentrations are $4.5(0.5) \times 10^{12}$, $9.0(1.0) \times 10^{12}$, and $4.5(0.5) \times 10^{13}$ cm^{-2}. Figure 5(a) presents the maximum photocurrent densities as 18.34, 15.87, and 9.09 nA m^{-1}, which appear at wavelengths of 459, 344, and 310 nm, respectively. The peaks of photocurrent density decrease obviously and the peak positions move towards the short-wave direction. The maximum photocurrent-density values indicate appealing photoelectric conversion performances. In addition, R_{ph} and EQE are calculated in Figs. 5(b)–5(d) and have similar trends. With increasing doping concentration, the maximum values of R_{ph} and EQE decrease. For $4.5(0.5) \times 10^{12}$ cm^{-2} doping concentration, this is suitable for blue-light detection, while the doping concentration of $9.0(1.0) \times 10^{12}$ and $4.5(0.5) \times 10^{13}$ cm^{-2} cases are suitable for UV detection. In addition, Fig. 5(d) reveals that the extinction ratio varies greatly with doping concentration. We can see that the extinction ratio of the device for $4.5(0.5) \times 10^{12}$ cm^{-2} doping concentrations can reach a maximum value of 21, which is advantageous for sensitivity to 459-nm-wavelength light. This indicates that the monolayer InSe-based *p-i-n* homojunction with low doping densities driven by photogalvanic effects is highly desirable for detection applications.

In Fig. 6, we contrast photocurrent density, R_{ph}, and EQE of the monolayer InSe-based *p-i-n* homojunction under different conditions. When applying a gate voltage of −2 V, the homojunction presents excellent performance and the photocurrent density, R_{ph}, and EQE reach 57.33 nA m^{-1}, 0.09 A W^{-1}, and 44%, respectively. Moreover, the substrate can result in interfacial charge redistribution, and the influence becomes larger with an increase of the dielectric constant; therefore, the maximum photocurrent values of Al_2O_3 and HfO_2 substrates reach 31.58 and 27.03 nA m^{-1}, respectively. The mobility increases with a decrease in doping concentration, leading to a low-doping-concentration *p-i-n* homojunction suitable for optical detector applications.

IV. CONCLUSION

We theoretically investigate the electronic properties of InSe through first-principles calculations. The monolayer InSe-based *p-i-n* homojunction has a built-in electric field and facilitates separate photogenerated electron-hole pairs. It exhibits a photocurrent density of 13.13 nA m^{-1} and R_{ph} of 0.022 A W^{-1} under the illumination of circularly polarized light. Also, the structure can induce a larger photocurrent density and high photoresponsivity through a low gate voltage or low doping concentration. Furthermore, the dielectric constant of the substrate affects the photocurrent spectral width from the visible-to-ultraviolet region with HfO_2 substrate. This work provides a route to design a photoelectric device based on the 2D semiconductor-based *p-i-n* homojunction.

ACKNOWLEDGMENTS

This research is supported by the National Natural Science Foundation of China (Grants No. 11904085 and No. 12074103), the Program for Outstanding Youth of Henan Province (Grant No. 202300410221), and the Henan Innovative Science and Technology Team (Grant No. CXTD2017080). The calculations are also supported by the High Performance Computing Center of Henan Normal University.

[1] L. Tong, Z. Peng, R. Lin, Z. Li, Y. Wang, X. Huang, K. H. Xue, H. Xu, F. Liu, H. Xia, *et al.*, 2D materials-based homogeneous transistor-memory architecture for neuromorphic hardware, Science **373**, 1353 (2021).

[2] J. W. Chen, S. T. Lo, S. C. Ho, S. S. Wong, T. H. Vu, X. Q. Zhang, Y. D. Liu, Y. Y. Chiou, Y. X. Chen, J. C. Yang, *et al.*, A gate-free monolayer WSe_2 *pn* diode, Nat. Commun. **9**, 3143 (2018).

[3] Z. Zhang, P. Chen, X. Duan, K. Zang, J. Luo, and X. Duan, Robust epitaxial growth of two-dimensional heterostructures, multiheterostructures, and superlattices, Science **357**, 788 (2017).

[4] S. Wu, Y. Chen, X. Wang, H. Jiao, Q. Zhao, X. Huang, X. Tai, Y. Zhou, H. Chen, X. Wang, *et al.*, Ultra-sensitive polarization-resolved black phosphorus homojunction photodetector defined by ferroelectric domains, Nat. Commun. **13**, 1 (2022).

[5] G. Wang, M. Zhang, D. Chen, Q. Guo, X. Feng, T. Niu, X. Liu, A. Li, J. Lai, D. Sun, *et al.*, Seamless lateral graphene *p-n* junctions formed by selective in situ doping for high-performance photodetectors, Nat. Commun. **9**, 5168 (2018).

[6] S. Ghosh, A. Varghese, K. Thakar, S. Dhara, and S. Lodha, Enhanced responsivity and detectivity of fast WSe_2 phototransistor using electrostatically tunable in-plane lateral *p-n* homojunction, Nat. Commun. **12**, 3336 (2021).

[7] M. Shimasaki, T. Nishihara, K. Matsuda, T. Endo, Y. Takaguchi, Z. Liu, Y. Miyata, and Y. Miyauchi, Directional exciton-energy transport in a lateral heteromonolayer of WSe_2-$MoSe_2$, ACS Nano **16**, 8205 (2022).

[8] L. Shu, L. Qian, X. Ye, and Y. Xie, Multifunctional Two-Dimensional $VSi_2N_4/WSi_2N_4/VSi_2N_4$ Photodetector Driven by the Photogalvanic Effect, Phys. Rev. Appl. **17**, 054010 (2022).

[9] C. Pan, C. Y. Wang, S. J. Liang, Y. Wang, T. Cao, P. Wang, C. Wang, S. Wang, B. Cheng, A. Gao, *et al.*, Reconfigurable logic and neuromorphic circuits based on electrically tunable two-dimensional homojunctions, Nat. Electron. **3**, 383 (2020).

[10] X. Wang, B. Wang, Q. Zhang, Y. Sun, E. Wang, H. Luo, Y. Wu, L. Gu, H. Li, and K. Liu, Grain-boundary engineering of monolayer MoS_2 for energy-efficient lateral synaptic devices, Adv. Mater. **33**, 2102435 (2021).

[11] X. Duan, C. Wang, J. C. Shaw, R. Cheng, Y. Chen, H. Li, X. Wu, Y. Tang, Q. Zhang, A. Pan, *et al.*, Lateral epitaxial growth of two-dimensional layered semiconductor heterojunctions, Nat. Nanotechnol. **9**, 1024 (2014).

[12] C. Zhang, M. Y. Li, J. Tersoff, Y. Han, Y. Su, L. J. Li, D. A. Muller, and C. K. Shih, Strain distributions and their influence on electronic structures of WSe_2-MoS_2 laterally strained heterojunctions, Nat. Nanotechnol. **13**, 152 (2018).

[13] Y. H. Chu, L. H. Wang, S. Y. Lee, H. J. Chen, P.-Y. Yang, C. J. Butler, L. S. Lu, H. Yeh, W. H. Chang, and M. T. Lin, Atomic scale depletion region at one dimensional $MoSe_2$-WSe_2 heterointerface, Appl. Phys. Lett. **113**, 241601 (2018).

[14] P. K. Sahoo, S. Memaran, Y. Xin, L. Balicas, and H. R. Gutierrez, One-pot growth of two-dimensional lateral heterostructures via sequential edge-epitaxy, Nature **553**, 63 (2018).

[15] R. Ma, H. Zhang, Y. Yoo, Z. P. Degregorio, L. Jin, P. Golani, J. Ghasemi Azadani, T. Low, J. E. Johns, L. A. Bendersky, *et al.*, $MoTe_2$ lateral homojunction field-effect transistors fabricated using flux-controlled phase engineering, ACS Nano **13**, 8035 (2019).

[16] S. V. Mandyam, M. Q. Zhao, P. Masih Das, Q. Zhang, C. C. Price, Z. Gao, V. B. Shenoy, M. Drndic, and A. T. C. Johnson, Controlled growth of large-area bilayer tungsten diselenides with lateral *p-n* junctions, ACS Nano **13**, 10490 (2019).

[17] E. Najafidehaghani, Z. Gan, A. George, T. Lehnert, G. Q. Ngo, C. Neumann, T. Bucher, I. Staude, D. Kaiser, T. Vogl, *et al.*, 1D *p-n* junction electronic and optoelectronic devices from transition metal dichalcogenide lateral heterostructures grown by one-pot chemical vapor deposition synthesis, Adv. Funct. Mater. **31**, 2101086 (2021).

[18] T. H. Tsai, Z. Y. Liang, Y. C. Lin, C. C. Wang, K. I. Lin, K. Suenaga, and P. W. Chiu, Photogating WS_2 photodetectors using embedded WSe_2 charge puddles, ACS Nano **14**, 4559 (2020).

[19] S. Jia, Z. Jin, J. Zhang, J. Yuan, W. Chen, W. Feng, P. Hu, P. M. Ajayan, and J. Lou, Lateral monolayer $MoSe_2$-WSe_2 *p-n* heterojunctions with giant built-in potentials, Small **16**, e2002263 (2020).

[20] A. Nipane, S. Jayanti, A. Borah, and J. T. Teherani, Electrostatics of lateral *p-n* junctions in atomically thin materials, J. Appl. Phys. **122**, 194501 (2017).

[21] H. Yu, A. Kutana, and B. I. Yakobson, Carrier delocalization in two-dimensional coplanar *p-n* junctions of graphene and metal dichalcogenides, Nano Lett. **16**, 5032 (2016).

[22] Y. An, Y. Hou, K. Wang, S. Gong, C. Ma, C. Zhao, T. Wang, Z. Jiao, H. Wang, and R. Wu, Multifunctional lateral transition-metal disulfides heterojunctions, Adv. Funct. Mater. **30**, 2002939 (2020).

[23] J. Balgley, J. Butler, S. Biswas, Z. Ge, S. Lagasse, T. Taniguchi, K. Watanabe, M. Cothrine, D. G. Mandrus, J. Velasco, Jr., *et al.*, Ultrasharp lateral *p-n* junctions in modulation-doped graphene, Nano Lett. **22**, 4124 (2022).

[24] E. G. Marin, D. Marian, M. Perucchini, G. Fiori, and G. Iannaccone, Lateral heterostructure field-effect transistors based on two-dimensional material stacks with varying thickness and energy filtering source, ACS Nano **14**, 1982 (2020).

[25] M. I. B. Utama, H. Kleemann, W. Zhao, C. S. Ong, F. H. da Jornada, D. Y. Qiu, H. Cai, H. Li, R. Kou, S. Zhao, *et al.*, A dielectric-defined lateral heterojunction in a monolayer semiconductor, Nat. Electron. **2**, 60 (2019).

[26] C. Xia, W. Xiong, J. Du, T. Wang, Y. Peng, Z. Wei, J. Li, and Y. Jia, Type-I transition metal dichalcogenides lateral homojunctions: Layer thickness and external electric field effects, Small **14**, e1800365 (2018).

[27] X. Wang, X. Zhou, A. Cui, M. Deng, X. Xu, L. Xu, Y. Ye, K. Jiang, L. Shang, L. Zhu, *et al.*, Flexo-photoelectronic effect in *n*-type/*p*-type two-dimensional semiconductors and a deriving light-stimulated artificial synapse, Mater. Horiz. **8**, 1985 (2021).

[28] S. Aftab, H. M. S. Ajmal, E. Elahi, H. M. Mansoor Ul Haque, Samiya, M. W. Iqbal, J. Aziz, S. Yousuf, M. Z. Iqbal, and M. A. Shehzad, Lateral PIN (p-$MoTe_2$/intrinsic-$MoTe_2$/n-$MoTe_2$) homojunction photodiodes, ACS Appl. Nano Mater. **5**, 6455 (2022).

[29] Y. Zhang, K. Ma, C. Zhao, W. Hong, C. Nie, Z. J. Qiu, and S. Wang, An ultrafast WSe_2 photodiode based on a lateral *p-i-n* homojunction, ACS Nano **15**, 4405 (2021).

[30] H. S. Lee, J. Y. Lim, S. Yu, Y. Jeong, S. Park, K. Oh, S. Hong, S. Yang, C. H. Lee, and S. Im, Seamless $MoTe_2$ homojunction PIN diode toward 1300 nm shortwave infrared detection, Adv. Opt. Mater. **7**, 1900768 (2019).

[31] Y. Zhang, W. Shen, S. Wu, W. Tang, Y. Shu, K. Ma, B. Zhang, P. Zhou, and S. Wang, High-speed transition-metal dichalcogenides based Schottky photodiodes for visible and infrared light communication, ACS Nano **16**, 19187 (2022).

[32] D. Wang, X. Liu, Y. Kang, X. Wang, Y. Wu, S. Fang, H. Yu, M. H. Memon, H. Zhang, W. Hu, *et al.*, Bidirectional photocurrent in *p-n* heterojunction nanowires, Nat. Electron. **4**, 645 (2021).

[33] D. Wu, M. Xu, L. Zeng, Z. Shi, Y. Tian, X. J. Li, C. X. Shan, and J. Jie, *In situ* fabrication of PdSe2/GaN Schottky junction for polarization-sensitive ultraviolet photodetection with high dichroic ratio, ACS Nano **16**, 5545 (2022).

[34] K. Thakar and S. Lodha, Multi-bit analog transmission enabled by electrostatically reconfigurable ambipolar and anti-ambipolar transport, ACS Nano **15**, 19692 (2021).

[35] S. B. Song, S. Yoon, S. Y. Kim, S. Yang, S. Y. Seo, S. Cha, H. W. Jeong, K. Watanabe, T. Taniguchi, G. H. Lee, *et al.*, Deep-ultraviolet electroluminescence and photocurrent generation in graphene/*h*BN/graphene heterostructures, Nat. Commun. **12**, 7134 (2021).

[36] S. Li, Z. Zhang, X. Chen, W. Deng, Y. Lu, M. Sui, F. Gong, G. Xu, X. Li, F. Liu, *et al.*, A high-performance in-memory photodetector realized by charge storage in a van der Waals MISFET, Adv. Mater. **34**, e2107734 (2022).

[37] X. Li, T. Liu, L. Li, M. He, C. Shen, J. Li, and C. Xia, Reconfigurable band alignment of m-GaS/n-XTe$_2$ (X = Mo, W) multilayer van der Waals heterostructures for photoelectric applications, Phys. Rev. B **106**, 125306 (2022).

[38] Y. Jiang, L. Zhang, R. Wang, H. Li, L. Li, S. Zhang, X. Li, J. Su, X. Song, and C. Xia, Asymmetric ferroelectric-gated two-dimensional transistor integrating self-rectifying photoelectric memory and artificial synapse, ACS Nano **16**, 11218 (2022).

[39] Y. Guo, S. Zhou, Y. Bai, and J. Zhao, Enhanced piezoelectric effect in Janus group-III chalcogenide monolayers, Appl. Phys. Lett. **110**, 163102 (2017).

[40] M. Wu, J. J. Shi, M. Zhang, Y. M. Ding, H. Wang, Y. L. Cen, and J. Lu, Enhancement of photoluminescence and hole mobility in 1- to 5-layer InSe due to the top valence-band inversion: Strain effect, Nanoscale **10**, 11441 (2018).

[41] D. A. Bandurin, A. V. Tyurnina, G. L. Yu, A. Mishchenko, V. Zolyomi, S. V. Morozov, R. K. Kumar, R. V. Gorbachev, Z. R. Kudrynskyi, S. Pezzini, *et al.*, High electron mobility, quantum Hall effect and anomalous optical response in atomically thin InSe, Nat. Nanotechnol. **12**, 223 (2017).

[42] J. Camassel, P. Merle, H. Mathieu, and A. Chevy, Excitonic absorption edge of indium selenide, Phys. Rev. B **17**, 4718 (1978).

[43] M. Brotons-Gisbert, D. Andres-Penares, J. Suh, F. Hidalgo, R. Abargues, P. J. Rodriguez-Canto, A. Segura, A. Cros, *et al.*, Nanotexturing to enhance photoluminescent response of atomically thin indium selenide with highly tunable band gap, Nano Lett. **16**, 3221 (2016).

[44] S. J. Magorrian, V. Zolyomi, and V. I. Fal'ko, Electronic and optical properties of two-dimensional InSe from a DFT-parametrized tight-binding model, Phys. Rev. B **94**, 245431 (2016).

[45] M. Brotons-Gisbert, R. Proux, R. Picard, D. Andres-Penares, A. Branny, A. Molina-Sanchez, J. F. Sanchez-Royo, and B. D. Gerardot, Out-of-plane orientation of luminescent excitons in two-dimensional indium selenide, Nat. Commun. **10**, 3913 (2019).

[46] G. Kresse, From ultrasoft pseudopotentials to the projector augmented-wave method, Phys. Rev. B **59**, 1758 (1998).

[47] G. Kresse, Efficient iterative schemes for ab initio total-energy calculations using a plane-wave basis set, Phys. Rev. B **54**, 11169 (1996).

[48] J. P. Perdew, K. Burke, and M. Ernzerhof, Generalized Gradient Approximation Made Simple, Phys. Rev. Lett. **77**, 3865 (1996).

[49] S. Smidstrup, *et al.*, QuantumATK: An integrated platform of electronic and atomic-scale modelling tools, J. Phys.: Condens. Matter **32**, 015901 (2020).

[50] M. Palsgaard, T. Markussen, T. Gunst, M. Brandbyge, and K. Stokbro, Efficient First-Principles Calculation of Phonon-Assisted Photocurrent in Large-Scale Solar-Cell Devices, Phys. Rev. Appl. **10**, 014026 (2018).

[51] M. Palsgaard, T. Gunst, T. Markussen, K. S. Thygesen, and M. Brandbyge, Stacked Janus device concepts: Abrupt *pn*-junctions and cross-plane channels, Nano Lett. **18**, 7275 (2018).

[52] Y. Gao, J. Liao, H. Wang, Y. Wu, Y. Li, K. Wang, C. Ma, S. Gong, T. Wang, X. Dong, *et al.*, Electronic Transport Properties and Nanodevice Designs for Monolayer $MoSi_2P_4$, Phys. Rev. Appl. **18**, 034033 (2022).

[53] J. Li, W. Liu, W. Zhou, J. Yang, H. Qu, Y. Hu, and S. Zhang, Dipole-Engineering Strategy for Regulating the Electronic Contact of a Two-Dimensional SbX/Graphene (X = P, As, Bi) van der Waals Interface, Phys. Rev. Appl. **17**, 054009 (2022).

[54] J. Hu, W. Xiong, C. Cai, J. Wang, J. Li, Y. Xie, and Y. Wang, Optical response of Te-based monolayer materials from first principles, Appl. Phys. Lett. **115**, 151104 (2019).

[55] J. Chen, Y. Hu, and H. Guo, First-principles analysis of photocurrent in graphene *PN* junctions, Phys. Rev. B **85**, 155441 (2012).

[56] H. Tang, B. Shi, Y. Wang, C. Yang, S. Liu, Y. Li, R. Quhe, and J. Lu, Layer-Dependent Photoabsorption and Photovoltaic Effects in Two-Dimensional Bi_2O_2X (X = S, Se, and Te), Phys. Rev. Appl. **15**, 064037 (2021).

[57] L. Zhang, K. Gong, J. Chen, L. Liu, Y. Zhu, D. Xiao, and H. Guo, Generation and transport of valley-polarized current in transition-metal dichalcogenides, Phys. Rev. B **90**, 195428 (2014).

[58] Q. Wang, J. Li, Y. Liang, B. Wang, and Y. Nie, BX_1-BX_2(X_1, X_2 = P, As, Sb) lateral heterostructure: Novel and efficient two-dimensional photovoltaic materials with ultra-high carrier mobilities, J. Mater. Chem. A **7**, 10684 (2019).

[59] Y. Yang, L. Zhang, J. Chen, X. Zheng, L. Zhang, L. Xiao, and S. Jia, An electrically switchable anti-ferroelectric bilayer In_2Se_3 based opto-spintronic device, Nanoscale **13**, 8555 (2021).

[60] X. Li, P. Yuan, L. Li, M. He, J. Li, and C. Xia, Sub-5-nm Monolayer GaSe MOSFET with Ultralow Subthreshold Swing and High *On*-State current: Dielectric Layer Effects, Phys. Rev. Appl. **18**, 044012 (2022).

[61] L. L. Gong, W. Xiong, Y. Q. Xie, J. Hu, P. Huang, and F. Wang, The large photoresponse and high polarization sensitivity of Te-based optoelectronic devices with the adsorbed hydroxide ions, Appl. Phys. Lett. **118**, 221109 (2021).

[62] C. Xia, J. Du, X. Huang, W. Xiao, W. Xiong, T. Wang, Z. Wei, Y. Jia, J. Shi, and J. Li, Two-dimensional n-InSe/p-GeSe(SnS) van der Waals heterojunctions: High carrier mobility and broadband performance, Phys. Rev. B **97**, 115416 (2018).

[63] H. L. Zhuang and R. G. Hennig, Single-layer group-III monochalcogenide photocatalysts for water splitting, Chem. Mater. **25**, 3232 (2013).

[64] J. Zhao, Y. Hu, Y. Xie, L. Zhang, and Y. Wang, Largely Enhanced Photogalvanic Effects in a Phosphorene

Photodetector by Strain-Increased Device Asymmetry, Phys. Rev. Appl. **14**, 064003 (2020).

[65] See the Supplemental Material at http://link.aps.org/supplemental/10.1103/PhysRevApplied.19.014039 for the optical absorption coefficient of monolayer InSe at the DFT-RPA level, the photocurrent density and R_{ph} of the monolayer InSe *p*-*i*-*n* homojunction, and other calculation results.

[66] X. Yang, X. Liu, L. Qu, F. Gao, Y. Xu, M. Cui, H. Yu, Y. Wang, P. Hu, and W. Feng, Boosting photoresponse of self-powered InSe-based photoelectrochemical photodetectors via suppression of interface doping, ACS Nano **16**, 8440 (2022).

[67] M. Long, A. Gao, P. Wang, H. Xia, C. Ott, C. Pan, Y. Fu, E. Liu, X. Chen, W. Lu, *et al.*, Room temperature high-detectivity mid-infrared photodetectors based on black arsenic phosphorus, Sci. Adv. **3**, e1700589 (2017).

[68] Y. Liu, Y. Cai, G. Zhang, Y. W. Zhang, and K. W. Ang, Al-doped black phosphorus *p*-*n* homojunction diode for high performance photovoltaic, Adv. Funct. Mater. **27**, 1604638 (2017).

[69] F. H. Koppens, T. Mueller, P. Avouris, A. C. Ferrari, M. S. Vitiello, and M. Polini, Photodetectors based on graphene, other two-dimensional materials and hybrid systems, Nat. Nanotechnol. **9**, 780 (2014).